DE GRUYTER Nanophotonics 2019; 8(12): 2235–2241

Research article

Kazuue Fujita*, Shohei Hayashi, Akio Ito, Masahiro Hitaka and Tatsuo Dougakiuchi

Sub-terahertz and terahertz generation in long-wavelength quantum cascade lasers

https://doi.org/10.1515/nanoph-2019-0238
Received August 8, 2019; revised October 11, 2019; accepted October 12, 2019

Abstract: Terahertz quantum cascade laser sources with intra-cavity non-linear frequency mixing are the first room-temperature electrically pumped monolithic semiconductor sources that operate in the 1.2–5.9 THz spectral range. However, high performance in low-frequency range is difficult because converted terahertz waves suffer from significantly high absorption in waveguides. Here, we report a sub-terahertz electrically pumped monolithic semiconductor laser. This sub-terahertz source is based on a high-performance, long-wavelength ($\lambda \approx 13.7$ μm) quantum cascade laser in which high-efficiency terahertz generation occurs. The device produces peak output power of 11 μW within the 615–788 GHz frequency range at room temperature. Additionally, a source emitting at 1.5 THz provides peak output power of 287 μW at 110 K. The generated terahertz radiation of <2 THz is mostly attributable to the optical rectification process in long-wavelength infrared quantum cascade lasers.

Keywords: difference frequency generation; integrated optics devices; intersubband transitions; quantum cascade laser; terahertz.

The terahertz (THz) spectral range has considerable potential for application in numerous fields, including communications, imaging, spectroscopy, and biological engineering [1, 2]. One major obstacle preventing the widespread commercial deployment of this technology is the lack of a compact and mass-producible high-performance semiconductor source operating in the THz range. THz quantum cascade lasers (QCLs) are promising candidate sources for the supply of intense coherent THz light [3–5]. The operating ranges of THz QCLs span from 1.2 to 5.4 THz, and these sources have been steadily developed in recent years [6–9]. However, the THz-QCL performance on the low-frequency side, in which there has been much previous research for THz applications, has been rather limited and the maximum operating temperature of low-frequency (<1.8 THz) QCLs was <100 K [4]. Additionally, further progress toward the development of QCL devices that emit at lower frequencies of <1 THz is difficult because population inversion is extremely challenging in low-frequency QCLs as a result of poor electron injection efficiency from the injector in the upper laser state and intersubband absorption in the injector. While sub-THz QCLs have been demonstrated, these devices require the application of a strong external magnetic field [10, 11].

THz QCL sources based on intra-cavity difference-frequency generation (DFG) [12], which were developed as alternative THz-QCL sources, are the only electrically driven monolithic semiconductor light sources that are capable of room-temperature operation in the THz spectral range [13–15]. Using the high design flexibility of QCL structures with giant second-order non-linear susceptibility [16], these devices have expanded spectral coverage that extends over nearly the entire 1–6 THz range [13–15]. Because this approach does not require population inversion to be maintained across the THz transitions in a QCL, THz-QCLs based on DFG may be suitable for lower-frequency THz generation. In fact, operation of a non-linear QCL source has been demonstrated at 1.2 THz using an external cavity setup [17]. However, extension of a non-linear QCL source to operation at lower frequencies means that major challenges must be overcome: THz generation efficiency is principally limited by the high free carrier absorption in the QCL waveguide and the THz frequency squared dependence of the DFG efficiency. Simultaneous achievement of high non-linearity for DFG and high mid-infrared (MIR) range pump powers is thus essential to compensate for the degradation in the DFG efficiency. Here, we report a sub-THz source based on a high-output-power QCL operating at $\lambda \approx 13.7$ μm. High MIR performance is achieved by the adoption of a dual-upper-state

---

***Corresponding author: Kazuue Fujita,** Central Research Laboratory, Hamamatsu Photonics K.K., 5000 Hirakuchi, Hamakita-ku, Hamamatsu 434-8601, Japan, e-mail: kfujita@crl.hpk.co.jp. https://orcid.org/0000-0002-1477-5187
Shohei Hayashi, Akio Ito, Masahiro Hitaka and Tatsuo Dougakiuchi: Central Research Laboratory, Hamamatsu Photonics K.K., 5000 Hirakuchi, Hamakita-ku, Hamamatsu 434-8601, Japan

(DAU) active region [18], which is designed to reduce optical losses in the active region while also having very high non-linear susceptibility [19–21]. This non-linear QCL device demonstrates a THz peak output power of 11 μW at room temperature (293 K) with multimode sub-THz emission at a frequency of approximately 700 GHz.

For high-power THz generation in a non-linear QCL source, high MIR pump powers are required. Currently, THz QCL sources with intra-cavity DFG were based on MIR-QCLs emitting in the 6–11 μm range, which can provide high performance. Long-wavelength MIR QCLs, in which wide quantum wells are used for the active region, can incorporate much higher optical non-linearity for THz DFG because of their increased values of transition dipole moments. However, the long-wavelength MIR QCLs reported to date have exhibited lower output powers because of high optical absorption occurring in the waveguide [22–24]. In this work, we adopt the DAU active region [18, 19] for longer wavelength emission, in which optical absorption can be reduced due to the electron transport dynamics [25, 26]. The conduction band diagram of the active region of the device is shown in Figure 1A. The waveguide core in the presented device consists of the DAU active region, which is designed for emission at around 14 μm for the 4-to-2 and 5-to-3 transitions in the labeled states shown in Figure 1A. To obtain higher population inversion in the long-wavelength QCL, the wavefunction of the lower upper state 4 is engineered to be localized in the first quantum well, while the transition from the higher upper state 5 is engineered to be vertical under the operating electric field. The lifetimes due to the longitudinal optical-phonon emissions are estimated to be $\tau_5 \approx 0.74$ ps and $\tau_4 \approx 1.65$ ps. Figure 1C shows the gain curve for the proposed device when calculated

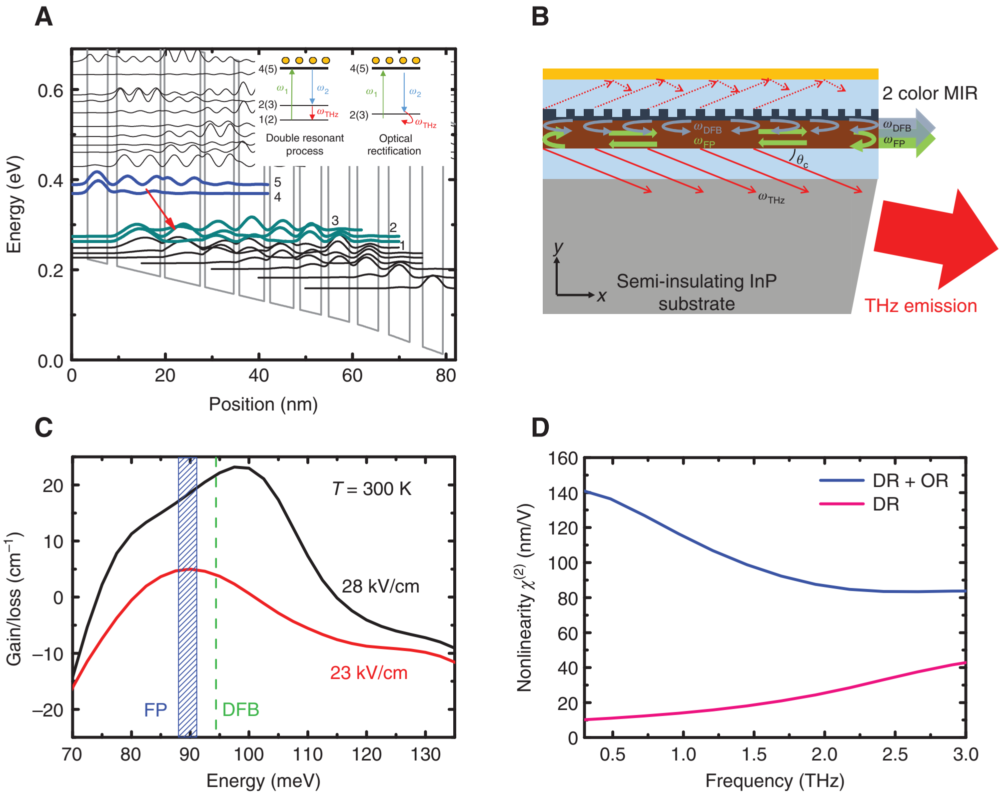

Figure 1: Design of sub-THz QCL source.
(A) Schematic conduction band diagram and squared moduli of the relevant wavefunctions of the injector/active/injector parts of the active region. An electric field of 28 kV/cm was applied to align the structure. The lattice-matched $In_{0.53}Ga_{0.47}As/In_{0.52}Al_{0.48}As$ layer sequence of a single period of the active layers starting from the injection barrier (i.e. toward the right) is given in angstroms as follows: **34**/43/**20**/93/**9**/76/**10**/62/**11**/54/**12**/51/**13**/46/<u>**15**/45/**17**/45</u>/**22**/45/**27**/44, where the InAlAs barrier layers are in bold, the InGaAs quantum well layers are in Roman type, and the doped layers (Si, 1.7×10^{17} cm^{-3}) are underlined. The schematics of the non-linear DFG processes for the double resonant process and for optical rectification are also shown in the inset. (B) Schematic of a distributed feedback/Fabry-Pérot configuration for non-linear THz-QCL. (C) Gain/absorption amplitude characteristics of the DAU active region design, calculated using the NEGF quantum transport code, along with the spectral positions of a single MIR pump frequency selected using a distributed feedback grating and the Fabry-Pérot modes of the second MIR pump as selected via the laser cavity. (D) Calculated optical non-linearity $\chi^{(2)}$ for the active region.

using the non-equilibrium Green's function (NEGF) calculation method [27, 28]. The anti-crossed DAUs are designed to produce a broader gain curve. In the presented device, the calculated absorption in the injector is estimated to be ~6 cm^{-1}.

The optical non-linearity $\chi^{(2)}$ in the intersubband transitions in the QCL active region is calculated using the summation of the two contributions of the double resonant (DR) and optical rectification (OR) processes. While the DR process was discussed in depth for previous non-linear QCLs, the importance of the OR process has only recently been indicated [29, 30]. The OR process was initially proposed for semiconductor quantum well structures [31, 32], and the intersubband transition process in quantum wells was then assessed by Dupont et al. [33]. For the 4-to-2 and 5-to-3 subband transitions in Figure 1A, electric charges are induced by off-resonant transitions due to two-color MIR pumps. The induced charges may produce a screening field that reduces the bias field. Consequently, one may expect the shift of the subband energies and changes in the dipole moments; these lead to optical non-linearity [31]. The coherent OR process may play an important role in the low-frequency range <3 THz because the DFG signal based on the DR process vanishes when the difference frequency is detuned from the energy spacing between the doublet states; in MIR QCL active regions, the energy spacing is larger than ~10 meV at all operating conditions, due to strong coupling in the miniband. While the DR process requires transitions between the three quantum states, as shown on the left in the inset of Figure 1A, the OR process relies on two quantum states, as illustrated on the right in the inset of Figure 1A. The simplified expression for $\chi^{(2)}$ is then given as follows:

$$\chi^{(2)} \approx \Delta N \frac{e^3}{\hbar^2 \varepsilon_0} \times \left(\begin{array}{l} \dfrac{-z_{21} z_{42} z_{41}}{(\omega_{\text{THz}} - \omega_{21} + i\Gamma_{21})(\omega_1 - \omega_{41} + i\Gamma_{41})} + \dfrac{-z_{21} z_{42} z_{41}}{(\omega_{\text{THz}} - \omega_{21} + i\Gamma_{21})(-\omega_2 - \omega_{41} + i\Gamma_{41})} \\ + \dfrac{-z_{32} z_{53} z_{52}}{(\omega_{\text{THz}} - \omega_{32} + i\Gamma_{32})(\omega_1 - \omega_{52} + i\Gamma_{52})} + \dfrac{-z_{32} z_{53} z_{52}}{(\omega_{\text{THz}} - \omega_{32} + i\Gamma_{32})(-\omega_2 - \omega_{52} + i\Gamma_{52})} \\ + \dfrac{z_{42}^2 (z_{44} - z_{22})}{(\omega_{42} - \omega_2 + i\Gamma_{42})(\omega_1 - \omega_{42} + i\Gamma_{42})} \dfrac{\omega_{\text{THz}} + i2\Gamma_{42}}{\omega_{\text{THz}} + i\Gamma} + \dfrac{z_{41}^2 (z_{44} - z_{11})}{(\omega_{41} - \omega_2 + i\Gamma_{41})(\omega_1 - \omega_{41} + i\Gamma_{41})} \dfrac{\omega_{\text{THz}} + i2\Gamma_{41}}{\omega_{\text{THz}} + i\Gamma} \\ + \dfrac{z_{53}^2 (z_{55} - z_{33})}{(\omega_{53} - \omega_2 + i\Gamma_{53})(\omega_1 - \omega_{53} + i\Gamma_{53})} \dfrac{\omega_{\text{THz}} + i2\Gamma_{53}}{\omega_{\text{THz}} + i\Gamma} + \dfrac{z_{52}^2 (z_{55} - z_{22})}{(\omega_{52} - \omega_2 + i\Gamma_{52})(\omega_1 - \omega_{52} + i\Gamma_{52})} \dfrac{\omega_{\text{THz}} + i2\Gamma_{52}}{\omega_{\text{THz}} + i\Gamma} \end{array} \right), \tag{1}$$

where ω_1 and ω_2 are the frequencies of the MIR pump powers; $\omega_{\text{THz}} = \omega_1 - \omega_2$ is the THz difference frequency; ΔN is the population inversion electron density; and z_{ij}, ω_{ij}, and Γ_{ij} are the transition dipole moments, transition frequencies, and transition linewidths between states *i* and *j*, respectively. The first four terms in the parenthesis of Eq. (1) corresponds to the DR process and the last four terms represent the OR process. Because all terms in the expression for $\chi^{(2)}$ are proportional to the product of three dipole moments, the very-long-wavelength infrared QCL active regions that consist of wide quantum wells lead to higher values of the dipole moments for the intersubband transitions, and this therefore results in high optical non-linearity for THz DFG. Figure 1D shows the calculated optical non-linearity $|\chi^{(2)}|$ for the DAU active region. By assuming the parameter values of $N \approx 1.1 \times 10^{15}$ cm^{-3}, $\Gamma = 8$ meV, and $\Gamma_{\text{ij}} = 4$ meV, we obtain $|\chi^{(2)}| = 12.3$ nm/V for the DR process and $|\chi^{(2)}| = 126$ nm/V for the contributions of both the DR and OR processes at 0.7 THz. At <1 THz, the non-linearity included in both the DR and OR terms is >10 times higher than the non-linearity calculated only with the DR terms.

In the experiments, our laser structure consists of a 70-stage $\text{In}_{0.53}\text{Ga}_{0.47}\text{As}/\text{In}_{0.52}\text{Al}_{0.48}\text{As}$ quantum cascade structure that was grown on a semi-insulating InP substrate by the metal-organic vapor phase epitaxy technique. The wafer was processed into buried-heterostructured waveguides with double-sided current extraction schemes. The growth process begins with a 200-nm-thick InGaAs current spreading layer (Si, 1.0×10^{18} cm^{-3}), and a 5.0-µm-thick n-InP (Si, 1.5×10^{16} cm^{-3}) film is used as a lower cladding layer. The lattice-matched InGaAs/InAlAs active regions were sandwiched between a 0.2-µm-thick n-$\text{In}_{0.53}\text{Ga}_{0.47}\text{As}$ layer (Si, 1.5×10^{16} cm^{-3}) and a 0.45-µm-thick n-$\text{In}_{0.53}\text{Ga}_{0.47}\text{As}$ layer (Si, 1.5×10^{16} cm^{-3}). The upper cladding layer consists of a 5-µm-thick n-InP (Si, 1.5×10^{16} cm^{-3}) followed by a 15-nm-thick n^{+}-InP (Si, ~10^{18} cm^{-3}) cap layer. The laser waveguide was designed to provide dielectric confinement for the MIR and Cherenkov THz DFG emissions into the semi-insulating InP substrate [13–15]. From the mode spacing $\Delta(1/\lambda)$ of the Fabry-Pérot (FP) laser, we find the MIR group index for our QCLs of $n_{\text{g}} = 3.46$; this is higher than that of the 8–11 µm QCLs ($n_g \approx 3.36$) that were previously used for the THz DFG. The group index of our device is much closer to the value of the THz refractive index ($n_{InP} \approx 3.52$) of the semi-insulating InP substrate. The front facet of the device was thus polished to 10°. A uniform single-period buried grating was defined for the single-wavelength emission.

Measurements of the sub-THz device were acquired using 200-ns current pulses at a 10-kHz repetition rate to gather both MIR and THz data. The emission spectra of the device were measured using a Fourier transform infrared spectrometer and recorded using a helium-cooled bolometer and a mercury cadmium telluride infrared detector for the THz and MIR components, respectively. Two off-axis parabolic mirrors with a focal length of 5 cm were used to collect and refocus the laser output onto a calibrated thermopile and the helium-cooled bolometer for the MIR and THz measurements, respectively. Optical filters were then used to distinguish between the output powers at the different frequencies. The MIR pump powers were corrected for the estimated 70% collection efficiency of our setup. The THz power was not corrected to account for the collection efficiency.

We used the distributed feedback (DFB)/FP pumping configuration, as shown in Figure 1B [20], for THz generation via two-color MIR non-linear mixing. Using this method, we have recently demonstrated the first THz frequency comb based on non-linear THz-QCL [15]. The grating period was designed to provide feedback single-mode lasing at the MIR wavelength for λ_{DFB} of ~13 µm. The spectral position of the DFB emission line was determined from the calculated gain curve shown in Figure 1C. A grating period of $\Lambda = 2.07$ µm was used for the DFB emission. A uniform single-period buried grating was defined for the single-wavelength emission and was etched to a depth of 200 nm into the upper n-$In_{0.53}Ga_{0.47}As$ waveguide layers. The grating coupling coefficient κ was calculated to be 4.5 cm^{-1}. The DFB position was detuned by approximately 30 cm^{-1} from the simulated peak gain at the threshold (23 kV/cm) so that it did not strongly suppress the FP emission, as shown in Figure 1B. The *I-L* characteristics for the MIR and THz signals for a 14-µm-wide, 3-mm-long, sub-THz device during pulsed operation are shown in Figure 2A. The THz emission threshold current density at 293 K was 3.6 kA/cm^2. Despite the long-wavelength MIR range, the total peak optical output power of 0.76 W with slope efficiency of 0.86 W/A was obtained at room temperature and two-wavelength emission was achieved at $\lambda_{DFB} = 13.14$ µm and $\lambda_{FP} = 13.7$ µm (inset, Figure 2A). The MIR slope efficiency of the presented device at room temperature is more than twice as high as the corresponding values of previously reported lasers operating within the same wavelength range [22–24]; these high slope efficiencies are attributed to the low waveguide losses in our device. Using room-temperature threshold currents for the devices with different cavity lengths, we obtained $\alpha_w \approx 9.1$ cm^{-1} for both at room temperature. After lasing at the shorter DFB emission wavelength λ_{DFB}, FP emission is observed. The MIR power increases as a function of input current up to the rollover point, and, as a result, peak THz power of approximately 11 µW is obtained. The inset in Figure 2A shows the MIR emission spectrum at 2.4 A and 293 K. Figure 2B shows the THz emission spectra at 293 K, which are a consequence of non-linear mixing between DFB single-mode lasing and multi-mode emission due to the FP cavity. The operating

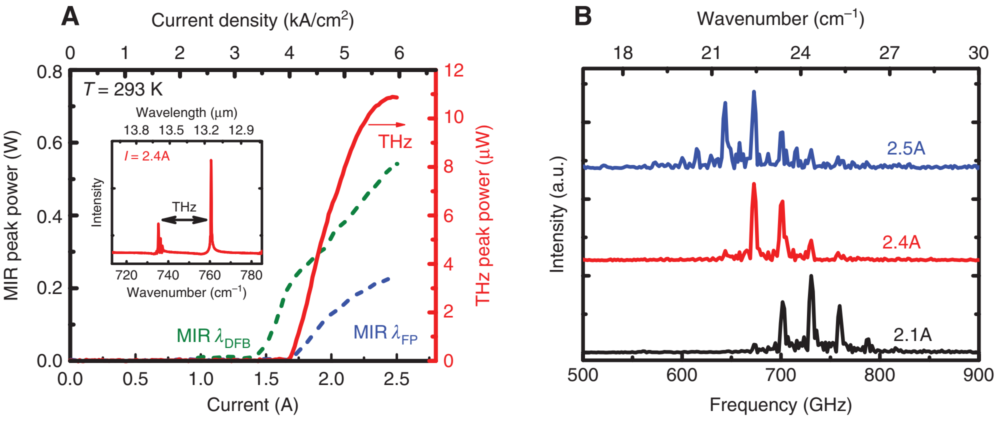

Figure 2: Room-temperature performance of a sub-THz source.
(A) Current-light output characteristics of a 3.0-mm-long, 14-µm-wide buried heterostructure device for THz peak power and MIR pump powers. The dashed blue line is the FP emission centered at 760 cm^{-1} and the dashed green line is DFB emission at 735 cm^{-1}. The laser was operated at room temperature with 200-ns pulses at 50 kHz. The room-temperature MIR emission spectrum is shown in the inset.
(B) Room-temperature THz emission spectra at various currents.

frequency range of 615–788 GHz at room temperature is the lowest among all electrically pumped monolithic THz laser sources, including THz-QCLs under a strong applied magnetic field at 215 K [11].

Figure 3A depicts the temperature dependence of the THz *I-V-L* characteristics, where *V* is the voltage, in the 78–293 K temperature range and in the same pulsed mode. The figure shows a THz output power of approximately 62 μW at 110 K at an emission frequency of ~0.9 THz. Figure 3B shows the THz and MIR spectra of the device when measured at different temperatures. Stable single-mode operation and multimode operation are obtained throughout the temperature range from 78 to 293 K. Figure 3C plots the THz power vs. the product of the two MIR pump powers. The MIR-to-THz power conversion efficiency, which is defined as the ratio of the THz peak power to the product of the MIR pump powers, was estimated to be >0.14 mW/W^2 at threshold at both 78 and 293 K. The higher THz output powers at low temperatures are thus attributed to the increased output pump power, as shown in the inset of Figure 3C.

We also fabricated devices with MIR DFB gratings designed for a pump frequency separation at 1.1, 1.4, and 2.4 THz. Figure 4A shows the room-temperature MIR and THz emission spectra of the devices, and the THz power as a function of the product of the MIR pump powers is shown in Figure 4B. The 1.1- and 1.4-THz devices provided 25 and 40 μW of powers with conversion efficiencies of 0.17 and 0.23 mW/W^2, and the 2.4-THz device demonstrated nearly 112 μW of power with a high conversion efficiency of 1.4 mW/W^2 at threshold. Figure 4C shows the conversion efficiencies as a function of operation frequency. The calculated curve including the OR and DR terms is in a reasonable agreement with the experimental results, in which the contribution of the DR term is negligibly small in the frequency range <2 THz, and thus the generated THz radiation is mostly attributable to the OR process. Further work is currently under way to understand the physics underlying the OR process in QCLs (Fujita K and Yamanishi M, unpublished).

Finally, we also tested the 1.1-THz source shown in Figure 4 at a low temperature of 110 K in order to obtain high peak output power in the 1 THz range. It would be

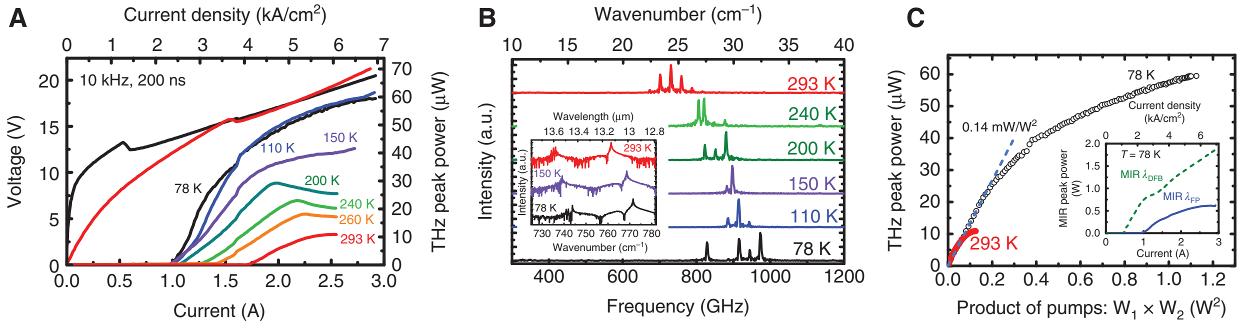

Figure 3: Temperature characteristics of the sub-THz source.
(A) Current-voltage-THz-light-output characteristics of a 3.0-mm-long, 14-μm-wide QCL source at different heat sink temperatures as measured in pulsed mode. (B) THz and MIR (inset) emission spectra of the device in (A) measured at different temperatures. (C) THz peak output power vs. the product of the MIR pump powers at 78 and 293 K. The MIR FP (blue solid line) and DFB pump powers (dashed lines) vs. the current density at 78 K are shown in the inset.

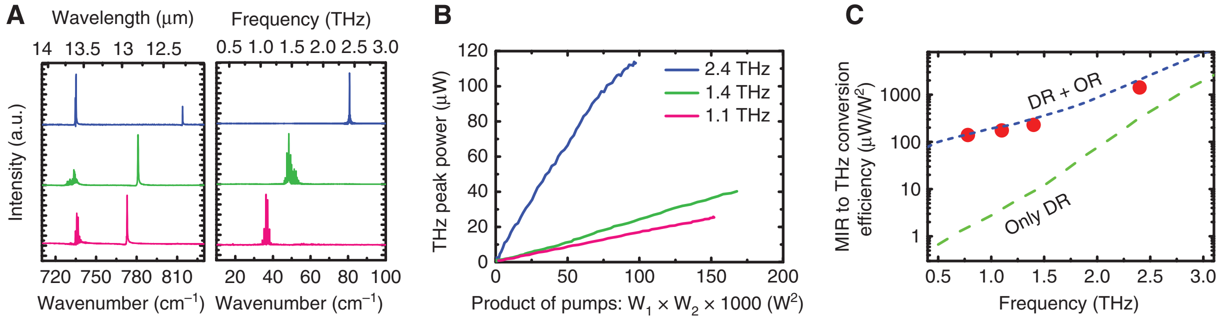

Figure 4: Room-temperature performance of 1.1-THz (red line), 1.4-THz (green line), and 2.4-THz (blue line) sources.
(A) MIR and THz spectra. (B) THz peak power output vs. the product of MIR pump powers. (C) The experiment and simulation results of the MIR-to-THz conversion efficiency.

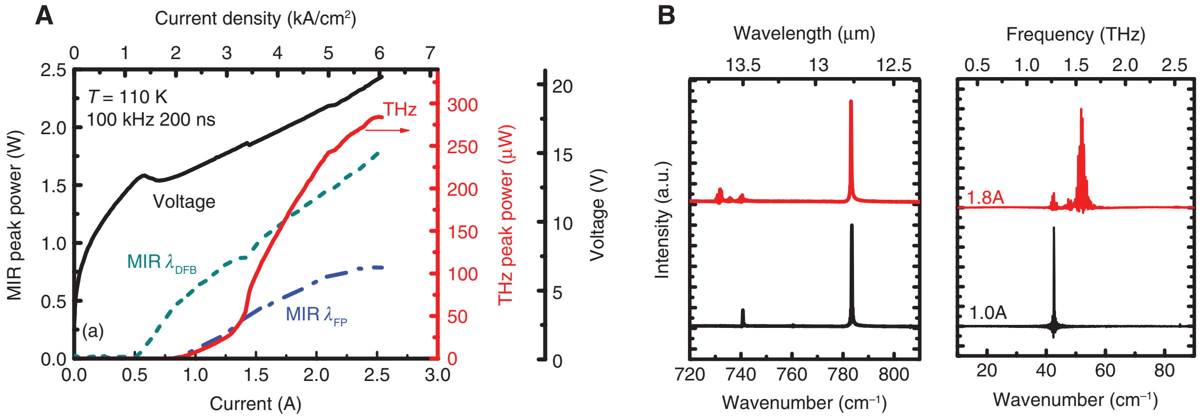

Figure 5: Device performance of the 1.1-THz source at 110 K.
(A) Current-voltage-light (*I-V-L*) output characteristics of the MIR (dashed lines, bottom and left axis) and THz emission (solid red line, bottom and right axis) of a 3-mm-long and 14-μm-wide QCL at 110 K with 200 ns pulsed at 100 kHz. (B) MIR and THz spectra at 110 K.

valuable to evaluate the performance of the low-frequency THz source at low temperatures, as the operation of THz-QCLs emitting at <1.8 THz has been rather limited. The THz light-current characteristics are shown in Figure 5A and B. The device provides THz peak power of approximately 287 μW, and the THz emission spans from 1.2 to 1.6 THz. The THz power at 110 K is comparable to the power of the 1.2–1.6 THz QCL at liquid helium temperature, which did not operate at >80 K [4]. We note that this device is capable of producing average power of >30 μW at higher duty cycles (>10%).

In conclusion, we report the realization of sub-THz sources based on high-power, long-wavelength MIR DAU-QCLs with a single DFB grating. We achieved a sub-THz emission frequency of ~700 GHz at room temperature, and we have demonstrated the lowest reported frequency (and longest wavelength) in any single monolithic semiconductor laser source. A 1.5-THz device produces an output power of 287 μW at 110 K, which is comparable to the performance of a low-frequency THz-QCL operating below the liquid nitrogen temperature. Furthermore, we experimentally clarified that the low-frequency THz generation in MIR QCLs is mostly attributed to the OR process for the intersubband optical non-linearity. The demonstrated low-frequency THz semiconductor sources, which are operable at room temperature, may offer new opportunities for many THz applications because the low-THz frequency range has previously lacked a high-performance semiconductor source. In fact, the first performance of THz imaging using the room-temperature THz-QCL source operating at a higher frequency has recently been demonstrated [34].

Acknowledgments: This work was supported by the Funder Id: http://dx.doi.org/10.13039/501100009105, Ministry of Internal Affairs and Communications/SCOPE #195006001. The authors thank Prof. M. Yamanishi and Dr. T. Edamura for their constructive suggestions and helpful comments, and Dr. K. Kuroyanagi for assistance with the operation of the silicon bolometer setup. KF expresses his thanks to Prof. M.A. Belkin of the University of Texas at Austin and Dr. S. Jung of TransWave Photonics LLC for insightful discussions about optical rectification in THz-QCL based on DFG.

References

[1] Dhillon SS, Vitiello MS, Linfield EH, et al. The 2017 terahertz science and technology roadmap. J Phys D Appl Phys 2017;50:043001.
[2] Tonouchi M. Cutting-edge terahertz technology. Nat Photonics 2007;1:97.
[3] Williams BS. Terahertz quantum-cascade lasers. Nat Photonics 2007;1:517.
[4] Walther C, Fischer M, Scalari G, Terazzi R, Hoyler N, Faist J. Quantum cascade lasers operating from 1.2 to 1.6 THz. Appl Phys Lett 2007;91:131122.
[5] Wienold M, Röben B, Lü X, et al. Frequency dependence of the maximum operating temperature for quantum-cascade lasers up to 5.4 THz. Appl Phys Lett 2015;107:202101.
[6] Zhou Z, Zhou T, Zhang S, et al. Multicolor T-ray imaging using multispectral metamaterials. Adv Sci 2018;5:1700982.
[7] Wan WJ, Li H, Cao JC. Homogeneous spectral broadening of pulsed terahertz quantum cascade lasers by radio frequency modulation. Opt Express 2018;26:980–9.
[8] Bosco L, Franckié M, Scalari G, Beck M, Wacker A, Faist J. Thermoelectrically cooled THz quantum cascade laser operating up to 210 K. Appl Phys Lett 2019;115:010601.
[9] Kainz MA, Semtsiv MP, Tsianos G, et al. Thermoelectric-cooled terahertz quantum cascade lasers. Opt Express 2019;27:20688–93.

[10] Scalari G, Turčinková D, Lloyd-Hughes J, et al. Magnetically assisted quantum cascade laser emitting from 740 GHz to 1.4 THz. Appl Phys Lett 2010;97:081110.

[11] Wade A, Fedorov G, Smirnov D, et al. Magnetic-field-assisted terahertz quantum cascade laser operating up to 225 K. Nat Photonics 2009;3:41.

[12] Belkin MA, Capasso F, Belyanin A, et al. Terahertz quantum-cascade-laser source based on intracavity difference-frequency generation. Nat Photonics 2007;1:288.

[13] Belkin MA, Capasso F. New frontiers in quantum cascade lasers: high performance room temperature terahertz sources. Phys Scr 2015;90:118002.

[14] Razeghi M, Lu QY, Bandyopadhyay N, et al. Quantum cascade lasers: from tool to product. Opt Express 2015;23:8462–75.

[15] Fujita K, Jung S, Jiang Y, et al. Recent progress in terahertz difference-frequency quantum cascade laser sources. Nanophotonics 2018;7:1795–817.

[16] Owschimikow N, Gmachl C, Belyanin A, et al. Resonant second-order nonlinear optical processes in quantum cascade lasers. Phys Rev Lett 2003;90:043902.

[17] Jiang Y, Vijayraghavan K, Jung S, et al. External cavity terahertz quantum cascade laser sources based on intra-cavity frequency mixing with 1.2–5.9 THz tuning range. J Opt 2014;16:094002.

[18] Fujita K, Edamura T, Furuta S, Yamanishi M. High-performance, homogeneous broad-gain quantum cascade lasers based on dual-upper-state design. Appl Phys Lett 2010;96:241107.

[19] Fujita K, Hitaka M, Ito A, et al. Terahertz generation in mid-infrared quantum cascade lasers with a dual-upper-state active region. Appl Phys Lett 2015;106:251104.

[20] Fujita K, Hitaka M, Ito A, Yamanishi M, Dougakiuchi T, Edamura T. Ultra-broadband room-temperature terahertz quantum cascade laser sources based on difference frequency generation. Opt Express 2016;24:16357–65.

[21] Kim JH, Jung S, Jiang Y, et al. Double-metal waveguide terahertz difference-frequency generation quantum cascade lasers with surface grating outcouplers. Appl Phys Lett 2018;113:161102.

[22] Fujita K, Yamanishi M, Edamura T, Sugiyama A, Furuta S. Extremely high T 0-values (~450 K) of long-wavelength (~15 μm), low-threshold-current-density quantum-cascade lasers based on the indirect pump scheme. Appl Phys Lett 2010;97:201109.

[23] Huang X, Charles WO, Gmachl C. Temperature-insensitive long-wavelength ($\lambda \approx 14$ μm) quantum cascade lasers with low threshold. Opt Express 2011;19:8297–302.

[24] Fuchs P, Semmel J, Friedl J, et al. Distributed feedback quantum cascade lasers at 13.8 μm on indium phosphide. Appl Phys Lett 2011;98:211118.

[25] Yamanishi M, Fujita K, Edamura T, Kan H. Indirect pump scheme for quantum cascade lasers: dynamics of electron-transport and very high T 0-values. Opt Express 2008;16:20748–58.

[26] Fujita K, Yamanishi M, Furuta S, Sugiyama A, Edamura T. Extremely temperature-insensitive continuous-wave quantum cascade lasers. Appl Phys Lett 2012;101:181111.

[27] Jirauschek C, Kubis T. Modeling techniques for quantum cascade lasers. Appl Phys Rev 2014;1:011307.

[28] Grange T. Electron transport in quantum wire superlattices. Phys Rev B 2014;89:165310.

[29] Burnett BA, Williams BS. Origins of terahertz difference frequency susceptibility in midinfrared quantum cascade lasers. Phys Rev Appl 2016;5:034013.

[30] Jung S, Jiang Y, Kim JH, et al. Narrow-linewidth ultra-broadband terahertz sources based on difference-frequency generation in mid-infrared quantum cascade lasers. In: Novel In-Plane Semiconductor Lasers XVI 2017 February 20, vol. 10123. International Society for Optics and Photonics, 2017:1012315.

[31] Yamanishi M. Field-induced optical nonlinearity due to virtual transitions in semiconductor quantum well structures. Phys Rev Lett 1987;59:1014.

[32] Chemla DS, Miller DA, Schmitt-Rink S. Generation of ultrashort electrical pulses through screening by virtual populations in biased quantum wells. Phys Rev Lett 1987;59:1018.

[33] Dupont E, Wasilewski ZR, Liu HC. Terahertz emission in asymmetric quantum wells by frequency mixing of midinfrared waves. IEEE J Quantum Electron 2006;42:1157–74.

[34] Nakanishi A, Fujita K, Horita K, Takahashi H. Terahertz imaging with room-temperature terahertz difference-frequency quantum-cascade laser sources. Opt Express 2019;27:1884–93.